Pure Appl. Chem., Vol. 80, No. 11, pp. 2451–2477, 2008.
doi:10.1351/pac200880112451

Microemulsion route to the synthesis of nanoparticles*

Ashok K. Ganguli‡, Tokeer Ahmad, Sonalika Vaidya, and Jahangeer Ahmed

Department of Chemistry, Indian Institute of Technology, Hauz Khas, New Delhi 110016, India

Abstract: Nanoparticles of several titanates and zirconates in the range of 20–60 nm have been obtained using the reverse micellar route. Important oxides like CeO_2 (mixture of nanorods; 7 nm diameter and 30 nm length and nanoparticles; 10 nm), ZrO_2 (3–4 nm) and SnO_2 (8 nm) have also been synthesized. Nanorods and nanoparticles of $CaCO_3$ in all three forms (aragonite, vaterite, and calcite) have been obtained using reverse micelles as nanoreactors. The specific reactions vary depending on the nature of the target nanomaterial. For synthesis of ternary oxides like $BaTiO_3$, a modified and convenient route using microemulsions (avoiding Ba-alkoxide) has evolved. Monophasic tin dioxide (SnO_2) was obtained when liquid NH_3 was used as precipitating agent. Transmission electron microscopy (TEM) studies show that the SnO_2 nanoparticles are highly uniform and particle size was found to be 6–8 nm at 500 °C. The gas sensing characteristics of SnO_2 have also been investigated using *n*-butane, which shows high sensitivity and fast recovery time. Reverse micelles have been used, for the first time, to mimic the conditions suitable for the room-temperature synthesis of the high-temperature and -pressure orthorhombic phase of calcium carbonate (aragonite). Other forms of calcium carbonate (vaterite and calcite) could be obtained by varying the atmospheric conditions. At a lower temperature (5 °C), homogeneous and monodisperse spheres of vaterite are obtained. The spherical particles aggregate after longer aging (168 h) to form nanorods, and the self-assembly is clearly seen at various stages by electron microscopy images. The samples were well characterized using powder X-ray diffraction (PXRD), line-broadening studies, TEM, variation in the dielectric properties with frequency and temperature, were measured on disks sintered at high temperature.

Keywords: microemulsion; dielectric material; gas sensing; particle synthesis; Mössbauer.

INTRODUCTION

Nanostructured materials have been fascinating the world of science and technology during the last 15 years because of their tremendous possibilities in generating novel shapes, structures, and the unusual phenomena associated with these materials. The characteristic length of these materials (at least one length) lies between 1–100 nm. This makes the properties of matter within this length scale significantly different from individual atoms or molecules and from bulk materials. Nanoparticles exhibit unique electronic, magnetic, optical, photonic, and catalytic properties [1,2], and their size is ideal for

*Paper based on a presentation at the 3rd International Symposium on Novel Materials and Their Synthesis (NMS-III) and the 17th International Symposium on Fine Chemistry and Functional Polymers (FCFP-XVII), 17–21 October 2007, Shanghai, China. Other presentations are published in this issue, pp. 2231–2563.

‡Corresponding author: Tel.: 91-11-26591511; Fax: 91-11-26854715; E-mail: ashok@chemistry.iitd.ernet.in

use as building blocks [3], which includes metals [4], semiconductors [5], core-shell nanostructures [6], and organic polymeric materials [7].

Metal oxide nanoparticles show interesting changes in their optical, magnetic, electrical, and catalytic properties accompanied by improved physical properties like mechanical hardness, thermal stability, or chemical passivity [8]. The properties of nanomaterials are influenced by the presence of a significant number of surface atoms and by the quantum confinement effect of the electronic states [9]. The potential applications for nanostructured oxide materials include paint pigments, cosmetics, pharmaceuticals, medical diagnostics, catalysts and supports, membranes and filters, batteries and fuel cells, electronics, magnetic and optical devices, flat panel displays, biomaterials, structured materials, and protective coatings [10].

SnO_2 is a wide-bandgap (3.6 eV) n-type semiconductor, widely used for gas sensors. Its unique conductance has been utilized for various applications such as gas sensors [11], microelectronics [12], solar cells [13], and photoelectrochemistry [14]. The compound has also been examined as a possible electrode material for lithium cells [15] and as photocatalysts [16]. As an n-type semiconductor, tin dioxide shows very high sensitivity toward reducing gases such as H_2, CO, hydrocarbons, and alcohol. It is known that the sensitivity can be improved by increasing the sensor surface area so as to increase the number of oxygen sites on the surfaces in these reducing gas species [11,17]. Thus, for application of tin dioxide as a sensing layer material of chemical gas sensors, a higher surface area of tin dioxide powder is desirable.

CeO_2 and ZrO_2 are refractory oxides with several applications. CeO_2 has been used in a variety of applications such as fuel cells [18], gas sensors [19], NO removal [20], counterelectrodes in smart window devices, and humidity sensors [21]. CeO_2 has a high refractive index, strong adhesion, and stability toward high temperature, chemical attack, and mechanical abrasion. Zirconia, a refractory material, is known to exist in three different structures viz. monoclinic (below 1170 °C, thermodynamically most stable form), tetragonal (between 1170–2370 °C), and cubic (above 2370 °C).

$SrTiO_3$, $PbTiO_3$, and Sr_2TiO_4 are important dielectric oxides used in electronic applications. $SrTiO_3$ shows very stable dielectric properties as a function of temperature and frequency. This makes a wide range of utility for these materials in the electronics industry [22–24]. Apart from its importance as a dielectric material, strontium titanate can also be used as a photocatalyst [25]. $BaTiO_3$ is a high dielectric constant material. It is widely used as a multilayer ceramic capacitor (MLCC). For increased miniaturization and volumetric efficiency of these multilayer capacitors, the thickness of the ceramic capacitor films has to be decreased. Another interest is to reduce the sintering temperature of $BaTiO_3$ to enable the use of more inexpensive non-noble metal electrodes. Both of these aspects put a greater emphasis on novel low-temperature synthetic approaches.

Barium orthotitanate (Ba_2TiO_4) is difficult to synthesize because it is not as stable as $BaTiO_3$. It is frequently formed as an intermediate during the preparation of $BaTiO_3$ powder by solid-state reaction of TiO_2 and $BaCO_3$ [26,27]. The presence of Ba_2TiO_4 as an impurity phase in $BaTiO_3$ leads to a decrease in the value of the dielectric constant at the Curie temperature. The presence of Ba_2TiO_4 also lowers the value of the Curie temperature [28]. Thus, it is important to understand the phase stability and dielectric properties of Ba_2TiO_4. Two structures viz. the low-temperature monoclinic ($P2_1/n$ space group) phase and the high-temperature orthorhombic phase ($P2_1nb$ space group) exist for Ba_2TiO_4 [29]. We could obtain both forms of Ba_2TiO_4 by the reverse micellar method.

Zirconates of alkaline earth metals such as $SrZrO_3$ and $BaZrO_3$ find importance in industry due to their applications as electronic ceramics [29], refractories [30], and heterogeneous catalysts [31]. $SrZrO_3$ exhibits orthorhombic symmetry [32] with space group of Pbnm. It is used extensively as a commercial ceramic dielectric material with high mechanical and chemical stability [33]. $BaZrO_3$ and $PbZrO_3$ are also important dielectric materials. The dielectric constant of $BaZrO_3$ ranges between 32–36 depending on the sintering temperature and the method of synthesis [34–36]. Lead zirconate, the first compound in which antiferroelectric (AFE) properties were discovered [37], crystallizes in an orthorhombic structure at room temperature [38], which transforms to a cubic structure at around

230 °C. It is used in capacitors and also in energy storage applications [39]. $BaZrO_3$ crystallizes in an ideal cubic (Pm3m) perovskite structure [38] at room temperature. Substitution of Ba ion in the Pb sites improves the dielectric properties of $PbZrO_3$ [40,41]. The Curie temperature shifts to a higher value [40,42] with an increase in the concentration of Pb ions in the Pb-rich region of $(Ba_{1-x}Pb_x)ZrO_3$. Here, we discuss a methodology to obtain the entire range of solid solution ($0 \le x \le 1$) for which pure phases have been obtained for the first time by using the reverse micellar route. Normal solid-state reactions yield either Ba- or Pb-rich compositions.

Calcium carbonate is a common mineral, which has continued to attract researchers because of its extraordinary diversity and its use in industry involved in the manufacture of medicine, paints, papers, rubber, plastics, pigments, cosmetics, etc. [43–45]. Among the three forms of $CaCO_3$ aragonite (orthorhombic), calcite (rhombohedral), and vaterite (hexagonal), the calcite form is the most stable, while aragonite is the high-pressure form of calcium carbonate. It is the main constituent of the shell of bivalve animals, corals, and beautiful pearls. The iridescent colors observed in shells of sea animals such as abalone [46] and in pearls are the result of deposition of minute layers of aragonite. Normally, aragonite has been obtained at a high pressure (6.16 GPa) and a temperature of 345 °C [47]. However, using a reverse micellar method, we could stabilize the pure aragonite state at room temperature.

The synthesis of nanoparticles involves the inhibition of growth of nanoparticles and the stabilization of nanoparticles against aggregation. In the recent past, several processes have been developed for the synthesis of nanomaterials. These processes include physical methods such as mechanical milling [48] and inert gas condensation [49], along with chemical methods such as oxidative precipitation [50], electrodeposition [51], hydrothermal [52], and sol-gel synthesis [53]. Among all the chemical processes, the microemulsion processing (reverse micelle synthesis) has been demonstrated as a very versatile and reproducible method [54–57]. This method is superior to many others in terms of being able to deliver homogeneous and monodisperse nanoparticles of a variety of metals [58,59], oxides [60,61], and chalcogenides [62]. The reaction takes place in the aqueous cores of the reverse micelles which are dispersed in an organic solvent and are stabilized by a surfactant. The dimensions of these aqueous cores are in the nanoregime and are thus being referred to as nanoreactors. The product obtained after the reaction is homogeneous. The other advantage of using this methodology is that the morphology of the product can also be controlled as the surfactant aggregates form a variety of structures which are used as templates. The size of the core of the reverse micelles can also be controlled by changing Wo ($[H_2O]$/[surfactant]). The advantage of this method is that it assumes a variety of structures depending on the constituents and the location within the phase diagram. Thus, the size and morphology of the product can be controlled by proper choice of the composition of the microemulsion system. The mechanism for the formation of nanocrystalline materials using reverse micelles is logical and simple. For the synthesis of a simple compound like AB, two identical microemulsions are prepared. Two different reactants (A and B) are introduced in these microemulsions. The two microemulsions are mixed by constant stirring. The collision of droplets results in the interchange of reactants, during which the reaction takes place inside the droplets which acts as nanoreactor. The two reverse micelles form the encounter pair (EP) which changes to fused dimer (FD) after collision. The surface tension of the FD becomes very high due to large surface area and it is unable to sustain its geometry. The FD breaks down into two stable smaller droplets containing the precipitated material.

Spontaneous formation of a microemulsion with a decrease in free energy is possible if the interfacial tension is low such that the remaining free energy of the interface is overcompensated by the entropy of dispersion of the droplets in the medium. Surfactants lower the interfacial tension, but in most cases the critical micellar concentration (CMC) or the limit of solubility is reached before the interfacial tension is close to zero. Addition of a second surfactant (cosurfactant) of a completely different nature then lowers the interfacial tension further. Cosurfactants are usually alcohols or amines where the number of carbon atoms in the alkyl group ranges from C_4 to C_{10}. A cosurfactant helps in the formation and stabilization of micelles or microemulsions by lowering the interfacial tension and thereby decreasing the free energy of the system.

In this review, we discuss the synthesis, structural characterization, and properties of $SrTiO_3$, $BaTiO_3$, Sr_2TiO_4, Ba_2TiO_4, $SrZrO_3$, (Ba, Pb)ZrO_3, CeO_2, ZrO_2, SnO_2, and $CaCO_3$. All these compounds were synthesized using the reverse micellar route. The compounds were studied by X-ray diffraction and transmission electron microscopy (TEM), and their detailed dielectric properties have also been investigated.

EXPERIMENTAL

The experimental section is divided into four parts dealing with the synthesis of (a) SnO_2, CeO_2 ZrO_2, (b) titanates, (c) zirconates, and (d) $CaCO_3$ nanoparticles. The details are shown in Table 1.

Table 1 Summarized experimental details of the compounds synthesized using reverse micellar route.

Compound	Surfactant system			Precursor	Washing solvent	Temp. for synthesis of pure phase (°C)
	Microemulsion A	Microemulsion B	Microemulsion C			
SnO_2	CTAB/1-butanol/ isooctane/0.1 M $SnCl_4 \cdot 5H_2O$	CTAB/1-butanol/ isooctane/0.1 M NH_3			1:1 $CHCl_3$/ methanol mixture	500
CeO_2	CTAB/1-butanol/ isooctane/0.1 M $Ce(NO_3)_3 \cdot 6H_2O$	CTAB/1-butanol/ isooctane/0.1 M $(NH_4)_2C_2O_4$		Cerium oxalate	1:1 $CHCl_3$/ methanol mixture	500
ZrO_2	CTAB/1-butanol/ isooctane/0.1 M Zirconium oxychloride	CTAB/1-butanol/ isooctane/0.1 M $(NH_4)_2C_2O_4$		Zirconium oxalate	1:1 $CHCl_3$/ methanol mixture	500
$SrTiO_3$	Tergitol/ 1-octanol/ cyclohexane/ 0.1 M strontium acetate	Tergitol/ 1-octanol/ cyclohexane/ 0.1 M Ti^{4+} soln.	Tergitol/ 1-octanol/ cyclohexane/ 0.1 M NaOH		Acetone	800
Sr_2TiO_4	Tergitol/ 1-octanol/ cyclohexane/ 0.1 M strontium acetate	Tergitol/ 1-octanol/ cyclohexane/ 0.1 M Ti^{4+} soln.	Tergitol/ 1-octanol/ cyclohexane/ 0.1 M NaOH		Acetone	800
Ba_2TiO_4	Tergitol/ 1-octanol/ cyclohexane/ 0.1 M barium acetate	Tergitol/ 1-octanol/ cyclohexane/ 0.1 M Ti^{4+} soln.	Tergitol/ 1-octanol/ cyclohexane/ 0.1 M NaOH		Acetone	1000
$SrZrO_3$	Tergitol/ 1-octanol/ cyclohexane/ 0.1 M strontium acetate	Tergitol/ 1-octanol/ cyclohexane/ 0.1 M zirconium oxychloride	Tergitol/ 1-octanol/ cyclohexane/ 0.1 M NaOH		Acetone	800

(*continues on next page*)

Table 1 (*Continued*).

Compound	Surfactant system			Precursor	Washing solvent	Temp. for synthesis of pure phase (°C)
	Microemulsion A	Microemulsion B	Microemulsion C			
$BaZrO_3$	Tergitol/ 1-octanol/ cyclohexane/ 0.1 M barium acetate	Tergitol/ 1-octanol/ cyclohexane/ 0.1 M zirconium oxychloride	Tergitol/ 1-octanol/ cyclohexane/ 0.1 M NaOH		Acetone	800
$PbZrO_3$	Tergitol/ 1-octanol/ cyclohexane/ 0.1 M lead acetate	Tergitol/ 1-octanol/ cyclohexane/ 0.1 M zirconium oxychloride	Tergitol/ 1-octanol/ cyclohexane/ 0.1 M NaOH		Acetone	800
$Ba_{1-x}Pb_xZrO_3$	Tergitol/ 1-octanol/ cyclohexane/ 0.1 M barium acetate	Tergitol/ 1-octanol/ cyclohexane/ 0.1 M lead acetate	Tergitol/ 1-octanol/ cyclohexane/ 0.1 M zirconium oxychloride (fourth microemulsion) Tergitol/ 1-octanol/ cyclohexane/ 0.1 M NaOH		Acetone	800

Tin dioxide nanoparticles were prepared from $SnCl_4 \cdot 5H_2O$ using the microemulsion system with cetyltrimethyl ammoniumbromide (CTAB), 1-butanol, and isooctane. The weight fractions of various constituents in these microemulsions were 16.76 % of CTAB, 13.90 % of 1-butanol, 59.29 % of isooctane, and 10.05 % of the aqueous phase. The other microemulsion contained 0.1 M NH_3 solution instead of $SnCl_4 \cdot 5H_2O$. Mixing the above two microemulsions and stirring overnight led to a precipitate which was separated by centrifugation and washing with 1:1 mixture of methanol and chloroform to remove residual hydrocarbons and the surfactant. The precipitate was dried in an oven at 60 °C, which on heating in air at 500 °C led to the formation of monophasic SnO_2.

CeO_2 nanoparticles were synthesized by the thermal decomposition of cerium oxalate precursors. The precursor oxalate was synthesized by the reverse micellar (microemulsion) route with CTAB as the surfactant, the cerium oxalate precursor was synthesized using two different microemulsions, one containing 0.1 M cerium nitrate hexahydrate and the other containing 0.1 M ammonium oxalate solution. The product was isolated by centrifugation and washed with 1:1 mixture of chloroform and methanol to remove residual hydrocarbons and the surfactant, and dried at room temperature. On heating the precursor at 500 °C, monophasic cerium oxide nanoparticles were obtained. Similarly, ZrO_2 nanoparticles were also obtained from the decomposition of zirconium oxalate. The synthetic methodology was the same as above where zirconyl oxychloride was used instead of cerium nitrate. The precursor was decomposed at 500 °C to obtain pure ZrO_2 nanoparticles.

For (b) (titanates), three different microemulsions containing Tergitol as the surfactant, 1-octanol as the cosurfactant, cyclohexane as the oil phase, and aqueous solutions were prepared, one for Ti^{4+}, the second containing the 0.1 M solution of metal ion and the third containing 0.1 M solution of NaOH as the precipitating agent. Ti^{4+} microemulsion was prepared as follows: 0.74 ml of Ti–isopropoxide

(Acros, 98+ %) was added to 7.4 ml of glacial acetic acid (Qualigens, LR grade, 99.5 %) under nitrogen atmosphere to yield hydroxyl titanium acylate. To this a small amount of distilled water was added which resulted in a white precipitate. The precipitate was dissolved in excess of distilled water, and the volume was made up to 25 mL. The three microemulsions were mixed and stirred for 15 h, after which cyclohexane was evaporated at 60 °C. The product was separated by centrifugation and washed with acetone to remove surfactant and the hydrocarbons present. Note that our report [63] on $BaTiO_3$ was the first to discuss the use of three different microemulsions to synthesize any nanomaterials. The pure titanantes were obtained at 800 °C. In the synthesis of Sr_2TiO_4 and Ba_2TiO_4, the volumes of Sr^{2+} or Ba^{2+} ion and hydroxy titanium acylate were adjusted in the ratio of 2:1 so that the desired stoichiometry is maintained. The rest of the procedure was similar as above. For (c) (zirconates) the procedure is same as for the titanates where the Ti^{4+} microemulsion is replaced by a Zr^{4+} containing microemulsions.

Nanocrystalline calcium carbonate, in all three forms (aragonite, vaterite, and calcite) was synthesized using the reverse micellar route with CTAB as the surfactant. The two microemulsions (containing Ca^{2+} and ammonium carbonate) were mixed slowly to give a white precipitate which was isolated by centrifugation. The precipitate was washed with 1:1 solvent mixture to remove residual hydrocarbons and the surfactant and dried in air. The optimal conditions of temperature and aging time for the formation of aragonite, vaterite, and calcite are shown in Table 2.

Table 2 Condition of temperature and aging time for the formation of vaterite, calcite, and aragonite phases.

Temperature (°C)	Aging time (h)	Vaterite phase (%)	Calcite phase (%)	Aragonite phase (%)
20	1	87.7	12.3	–
20	8	87.7	12.3	–
20	44	66.7	33.3	–
20	54	56.5	43.5	–
20	96	26	74	–
20	168	–	100	–
40(±3)	6	–	–	100
60(±2)	6	–	–	100
70(±1)	6	–	–	100
85(±1)	6	–	–	100
105(±2)	6	–	100	–
5	6	74	26	–
12	18	92.6	7.4	–

Powder X-ray diffraction (PXRD) studies were carried out on a Bruker D8 Advance diffractometer using Ni-filtered Cu Kα radiation. Typically, scans were recorded with a step size of 0.02° and step time of 1 s. The data was subjected to background correction and the $K\alpha_2$- reflections were removed. The grain size was calculated using Scherrer's method. The cell parameters were determined using a least-square fitting procedure on all reflections using quartz as the external standard. The dielectric measurements were carried out on sintered disks (~93–95 % of the theoretical density) using Hewlett Packard 4284L multifrequency LCR meter in the range of 50 Hz to 500 kHz. Temperature variation studies of the dielectric constant and dielectric loss were carried out in the range of 35–300 °C. TEM studies for all the above compounds were carried out using a Tecnai-20 G^2 electron microscope operating at 200 kV. Infrared (IR) studies were carried out on a Nicolet Protege 460 FTIR Spectrometer. For gas sensing study, a thick paste of the powder was made with diluted alumina sol. The paste was applied on the outer surface of thin alumina tubes containing Kanthal heating coils placed inside the tube (length 3 mm, outer diameter 2 mm, and thickness 0.5 mm) with gold electrodes and platinum lead wires for electrical contact. The samples were dried and cured at 650 °C for 30 min. The electrical re-

sistance of the coatings and their response to 1000 ppm *n*-butane were measured at 350 °C using a digital multimeter. The measurement system was calibrated using a standard LPG sensor of FIGARO, Japan.

RESULTS AND DISCUSSION

Structural characterization

Figure 1 shows the PXRD patterns of SnO_2 nanoparticles obtained by the reverse micellar method and heated at 500 °C. The average size was found to be 6–8 nm from TEM studies (inset of Fig. 1) which matches the crystallite size calculated by Scherrer's equation. It may be noted that samples with 3–4 nm would be preferred for gas sensing properties as grains less than 6 nm in diameter would have high sensitivity. It is known that the Schottky barrier is close to 3 nm, and particle sizes less than twice the Schottky barrier are more sensitive [64]. Fourier transform–infrared (FT–IR) studies of SnO_2 (inset of Fig. 2), show absorptions at ~3341 and ~1630 cm^{-1} which correspond to the stretching vibration of –OH group and the bending vibration of adsorbed molecular water, respectively [65]. The strong bands near 633 cm^{-1} correspond to the stretching vibrations of Sn–O, which indicates that SnO_2 is well-crystalline. Weak bands at 1393 and 2921 cm^{-1} corresponding to the bending vibration of $-CH_2$ and the stretching vibration of –C–H band [66] arising due to the surfactant molecules associated with SnO_2 can also be seen.

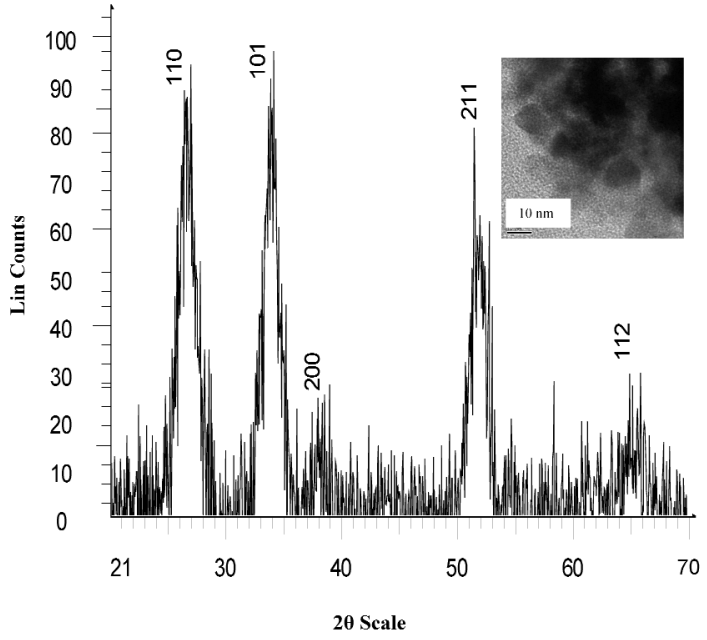

Fig. 1 PXRD patterns of SnO_2 nanoparticles. Inset shows TEM image of SnO_2 nanoparticles.

The Mössbauer spectrum of SnO_2 nanoparticles (Fig. 2) shows a very small isomer shift (0.04 mm/s) with respect to bulk SnO_2 along with a quadrupole splitting (QS) of 0.49 mm/s. Bulk SnO_2 gives a negligible QS (0.06 mm/s). The small isomer shift detected in the nanoparticles of SnO_2 indicates an enhancement of s-electron density in comparison with the bulk, which indicates a small variation in the nature of Sn–O bonding in nanosized SnO_2. The moderate QS (0.49 mm/s) observed in the nanosized SnO_2 indicates lowering of the symmetry around the tin atoms, which may be attributed to

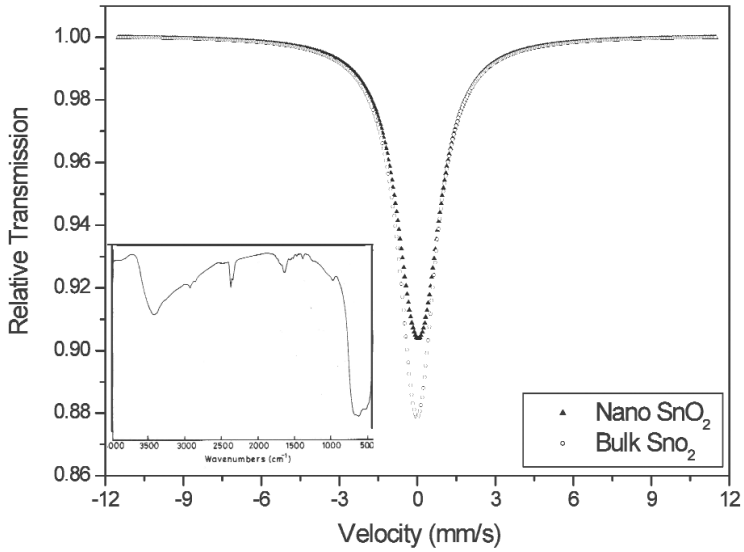

Fig. 2 Mössbauer spectra of SnO_2 nanoparticles and bulk SnO_2. Inset shows the FT–IR spectra of SnO_2 nanoparticles obtained at 500 °C.

oxygen vacancies [67]. Because of the characteristic broad line width of SnO_2, the changes in the isomer shift observed in the nano form are not apparently visible and could be extracted through a curve fitting procedure.

Cubic CeO_2 was obtained after decomposition of the oxalate precursor (obtained using reverse micelles) at 500 °C. The PXRD pattern for CeO_2 is shown in Fig. 3. The crystallite size for CeO_2 was

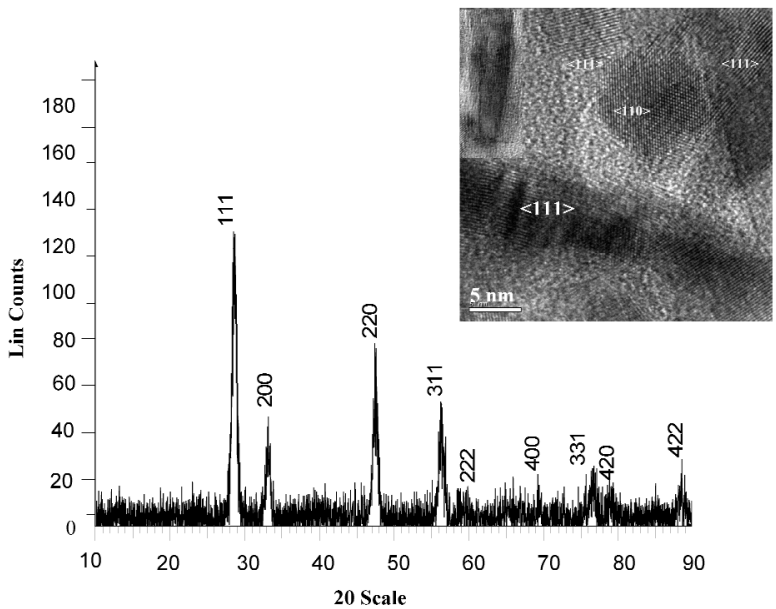

Fig. 3 PXRD pattern of CeO_2 obtained by the decomposition of cerium oxalate at 500 °C. Inset shows high-resolution TEM (HR-TEM) images of cerium oxide (from the oxalate precursor) showing the presence of nanorods and nanoparticles.

15 nm. Mixture of particles (10 nm in size) and rods (7 nm diameter and 30 nm length) were observed for CeO_2 (inset of Fig. 3).

We have also synthesized zirconium oxalate using reverse micelles. XRD studies show that the phase was amorphous. Tetragonal ZrO_2 (12 nm crystallite size) (Fig. 4a) with minor impurity of monoclinic phase (10 %) was obtained when the zirconium oxalate precursor was heated at 500 °C for 6 h. The refined unit cell parameters were calculated for the tetragonal cell as a = 3.957(9) Å, c = 5.16(3) Å. The particle size from TEM studies (inset of Fig. 4a) was found to vary from 3 to 5 nm. We have been successful in stabilizing the higher-temperature tetragonal phase at low temperature (tetragonal phase is normally stabilized between 1170–2370 °C). The size distribution plot (calculated from TEM) is shown in Fig. 4b.

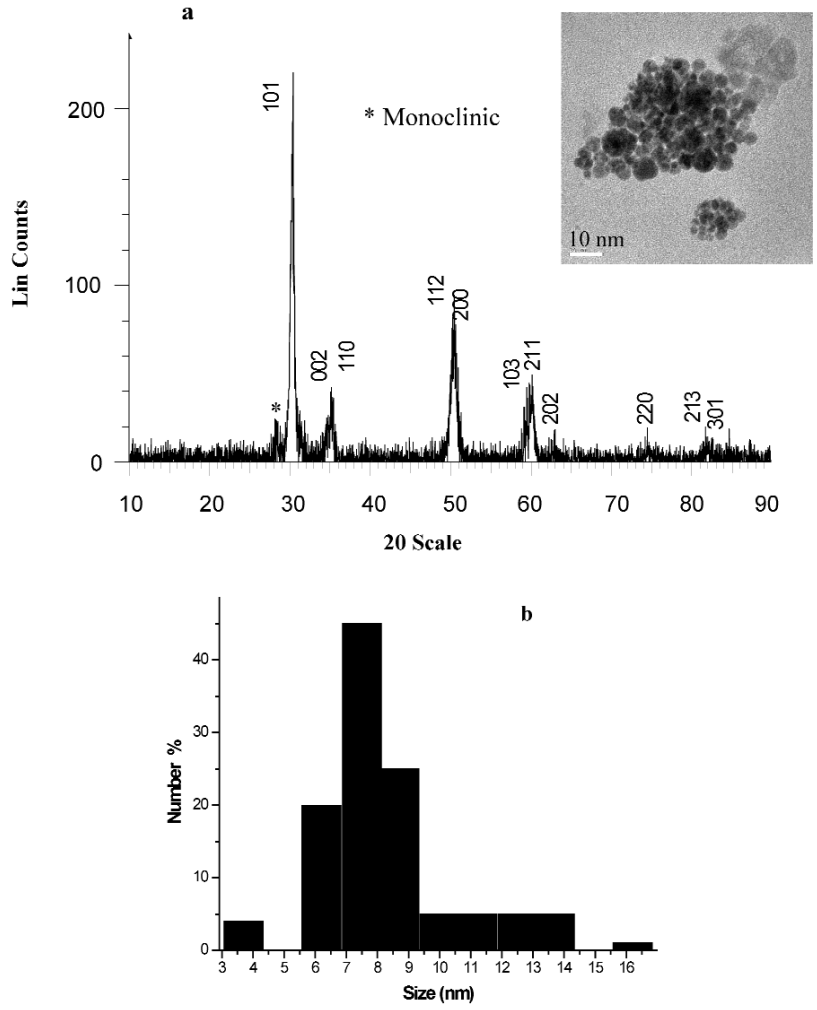

Fig. 4 (a) PXRD pattern of ZrO_2 obtained by the decomposition of zirconium oxalate at 500 °C. Inset shows TEM image of zirconium oxide (from the oxalate precursor). (b) Size distribution plot of ZrO_2 nanoparticles.

Several titanates related to perovskite structure were obtained using reverse micelles. Pure $SrTiO_3$ phase (Fig. 5a) was obtained after heating the powder (obtained by the reverse micellar route). $SrTiO_3$ (cubic) with refined lattice parameter of a = 3.9060(7) Å and crystallite size (obtained by X-ray line-

broadening) of 35 nm was obtained. TEM studies (inset of Fig. 5a) of $SrTiO_3$ show grain size of 50 nm. The size distribution plot (calculated from TEM) is shown in Fig. 5b. On carrying out reactions with 2:1 stoichiometry of Sr:Ti pure Sr_2TiO_4 could be obtained at 800 °C. All the reflections in the PXRD pattern, as shown in Fig. 6a, could be indexed on the basis of a tetragonal cell with the refined lattice parameters of a = 3.8821(8) Å and c = 12.574(5) Å with a crystallite size of 25 nm. TEM studies (inset of Fig. 6a) show grains of the size 20–25 nm for pure Sr_2TiO_4. The size distribution plot (calculated from TEM) is shown in Fig. 6b.

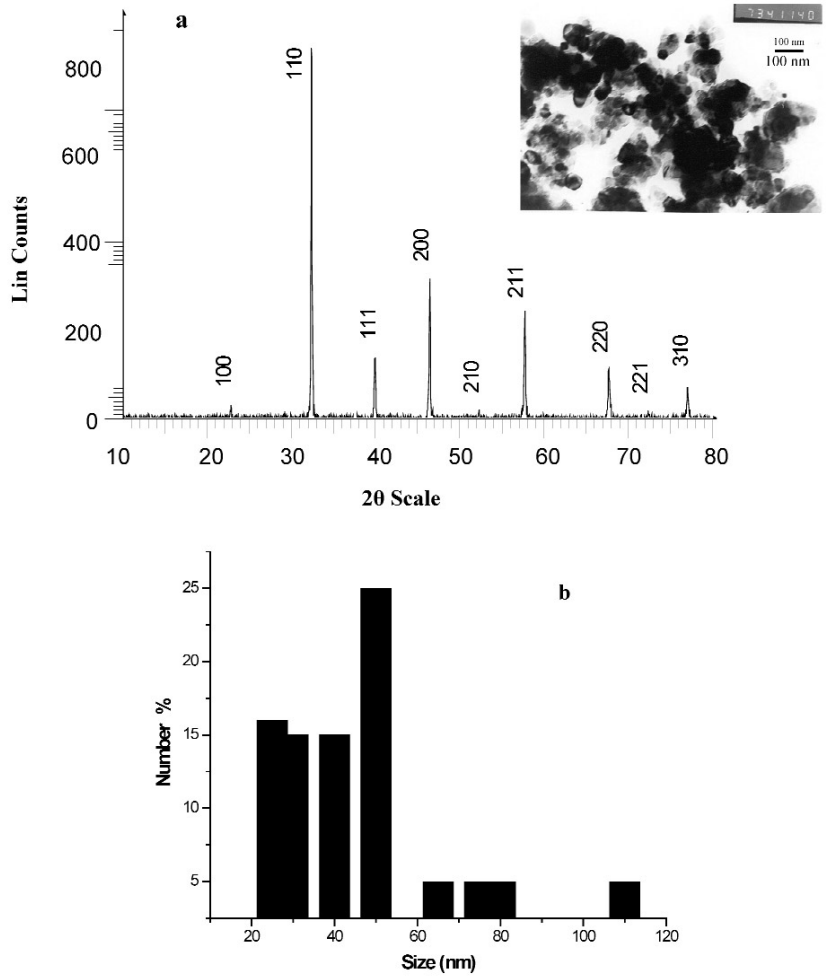

Fig. 5 (a) PXRD pattern of $SrTiO_3$ obtained by heating the precursor at 800 °C. Inset shows TEM image of $SrTiO_3$ powder after heating at 800 °C. (b) Size distribution plot of $SrTiO_3$.

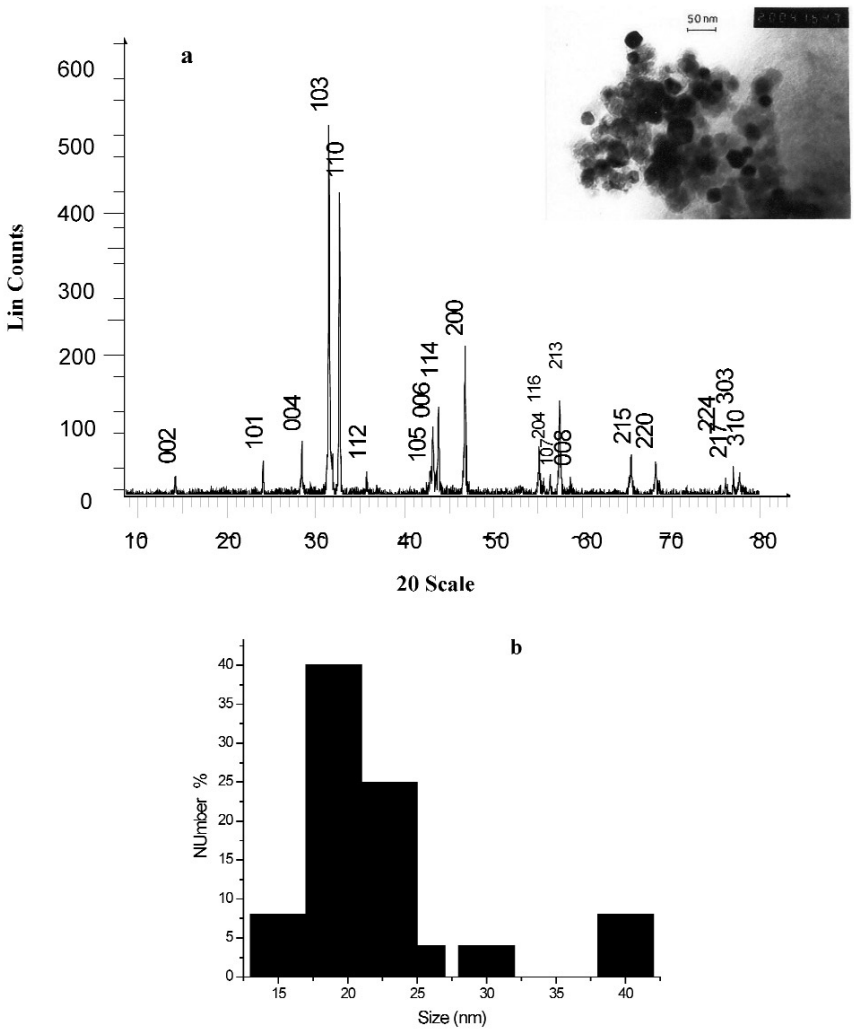

Fig. 6 (a) PXRD patterns of Sr_2TiO_4 after calcining at 800 °C. Inset shows TEM micrograph of Sr_2TiO_4 powder after heating at 800 °C. (b) Size distribution plot of Sr_2TiO_4.

Monophasic $BaTiO_3$ could also be obtained after heating the precursor at 800 °C (Fig. 7a). The XRD pattern could be indexed on a tetragonal cell, and a crystallite size of 20 nm was deduced from X-ray line-broadening studies. The grain size (inset of Fig. 7a) was found to be 20–25 nm from TEM studies. Nanocrystalline $BaTiO_3$ has been synthesized by reverse micellar method by using a single microemulsion as a reaction chamber as reported by some reports [68–70]. Here, the alkoxide mixture of barium and titanium was hydrolyzed to obtain the pure powder. A sizable number of agglomerated grains was reported, which could be due to the use of a single microemulsion. In our studies, we have used three different microemulsions for the two metal ions (Ba^{2+}, Ti^{4+}) and the precipitating agent (NaOH). The idea behind this modified route was to minimize the agglomeration and to achieve the monodispersity as well as uniformity of the grains. Note that we have also avoided the use of air-sensitive and expensive Ba-alkoxide as a starting reagent. The size distribution plot (calculated from TEM) is shown in Fig. 7b.

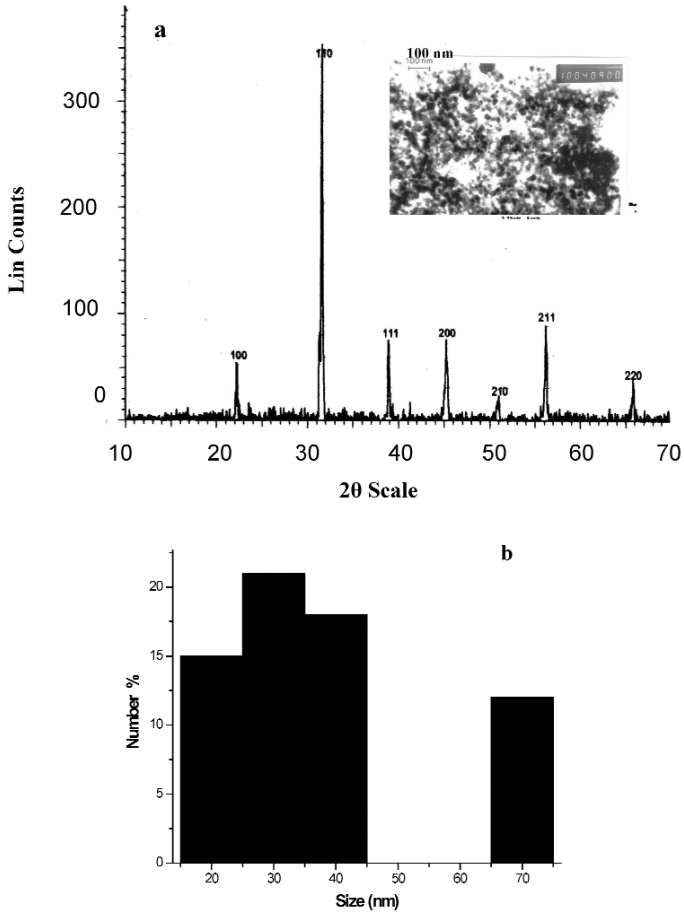

Fig. 7 (a) PXRD pattern of $BaTiO_3$ after calcining at 800 °C. Inset shows TEM micrograph of $BaTiO_3$ at 800 °C. (b) Size distribution plot of $BaTiO_3$.

We could also synthesize the 2:1 phase (Ba_2TiO_4) using the appropriate starting stoichiometry by the reverse micellar method. The PXRD pattern of the oxide (obtained at 1000 °C) (Fig. 8a) could be indexed on the basis of an orthorhombic cell with the refined lattice parameters of a = 6.101(2) Å, b = 22.94(1) Å, c = 10.533(2) Å. The grain size for the same was found to vary between 150–200 nm (inset of Fig. 8a). The size distribution plot (calculated from TEM) is shown in Fig. 8b.

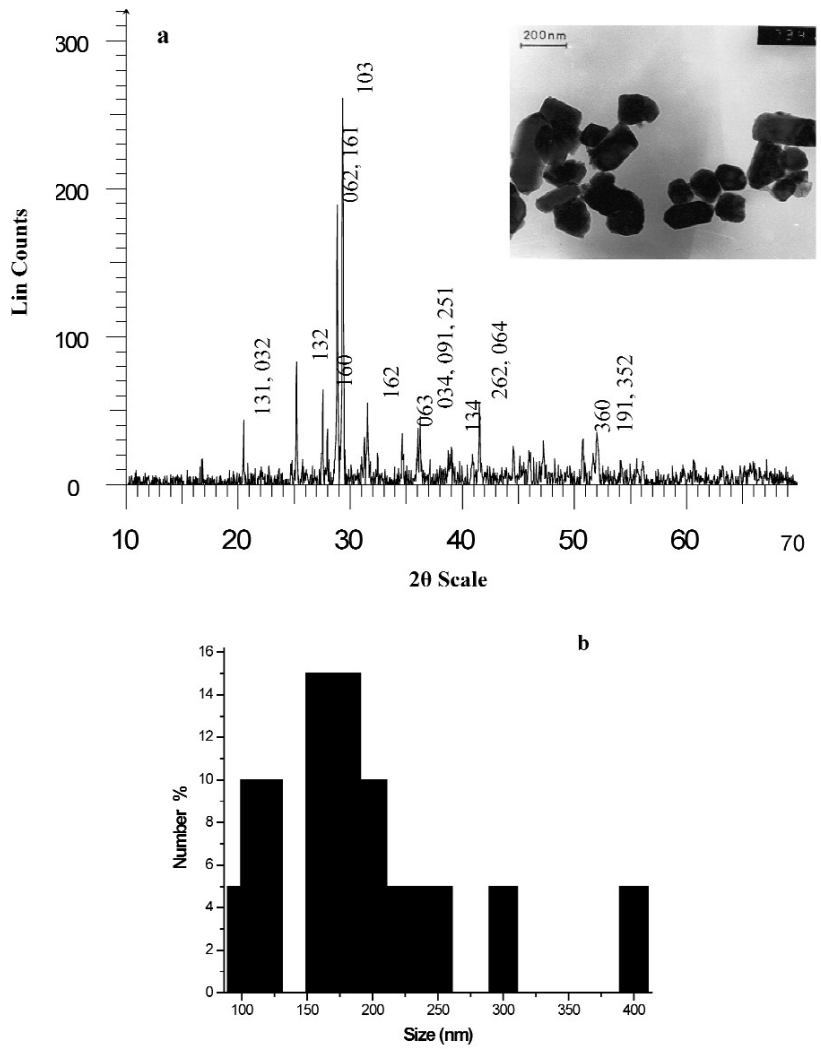

Fig. 8 (a) PXRD pattern of Ba_2TiO_4 after calcining at 1000 °C. Inset shows TEM micrograph of Ba_2TiO_4 heated at 1000 °C. (b) Size distribution plot of Ba_2TiO_4.

The precursor obtained from the microemulsions of Sr^{2+} and Zr^{4+} after centrifugation was found to be amorphous. After heating at 500 °C, the XRD pattern showed reflections corresponding to $SrCO_3$ and ZrO_2. Monophasic $SrZrO_3$ with a crystallite size of 62 nm was obtained after heating at 800 °C. The XRD pattern (Fig. 9a) could be indexed on the basis of an orthorhombic cell as is known for $SrZrO_3$ (JCPDS No. 10-0268) with the refined lattice parameters of a = 5.802(3) Å, b = 8.172(8) Å, and c = 5.77(1) Å. The grain size was found to be 65–75 nm (after heating at 800 °C) from the TEM studies, as shown in the inset of Fig. 9a. The size distribution plot (calculated from TEM) is shown in Fig. 9b.

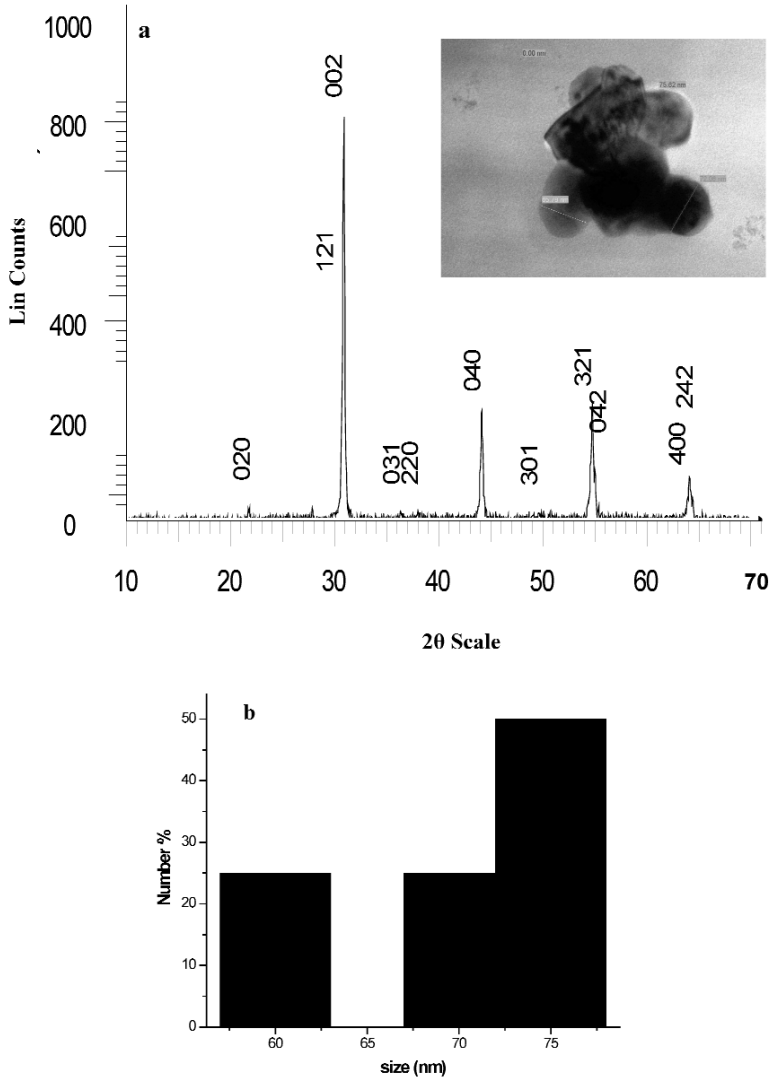

Fig. 9 (a) PXRD pattern of $SrZrO_3$ after calcining at 800 °C. Inset shows TEM micrograph of $SrZrO_3$ heated at 800 °C. (b) Size distribution plot of $SrZrO_3$.

Monophasic $BaZrO_3$ and $PbZrO_3$ with a crystallite size of 35 and 50 nm, respectively, were also obtained after heating the centrifuged precursor at 800 °C. $BaZrO_3$ was indexed on the basis of a cubic cell with the refined lattice parameter a = 4.1803(2) Å (Fig. 10a). PXRD studies also show a similar pattern after sintering the $BaZrO_3$ powder at 1000 °C. For $PbZrO_3$ (Fig. 11a), all the reflections could be indexed on an orthorhombic cell with the refined lattice parameters of a = 5.8621(5) Å, b = 11.791(3) Å, and c = 8.243(2) Å. PXRD studies show no change in the pattern after sintering the powder at 1000 °C. Particles of size 25–30 nm for $BaZrO_3$ (inset of Fig. 10a) and 75 nm for $PbZrO_3$ (inset of Fig. 11a) were found using TEM studies. The ED pattern (inset of Fig. 11) matches with orthorhombic $PbZrO_3$. The size distribution plot of $BaZrO_3$ and $PbZrO_3$ (calculated from TEM) is shown in Figs. 10b and 11b, respectively.

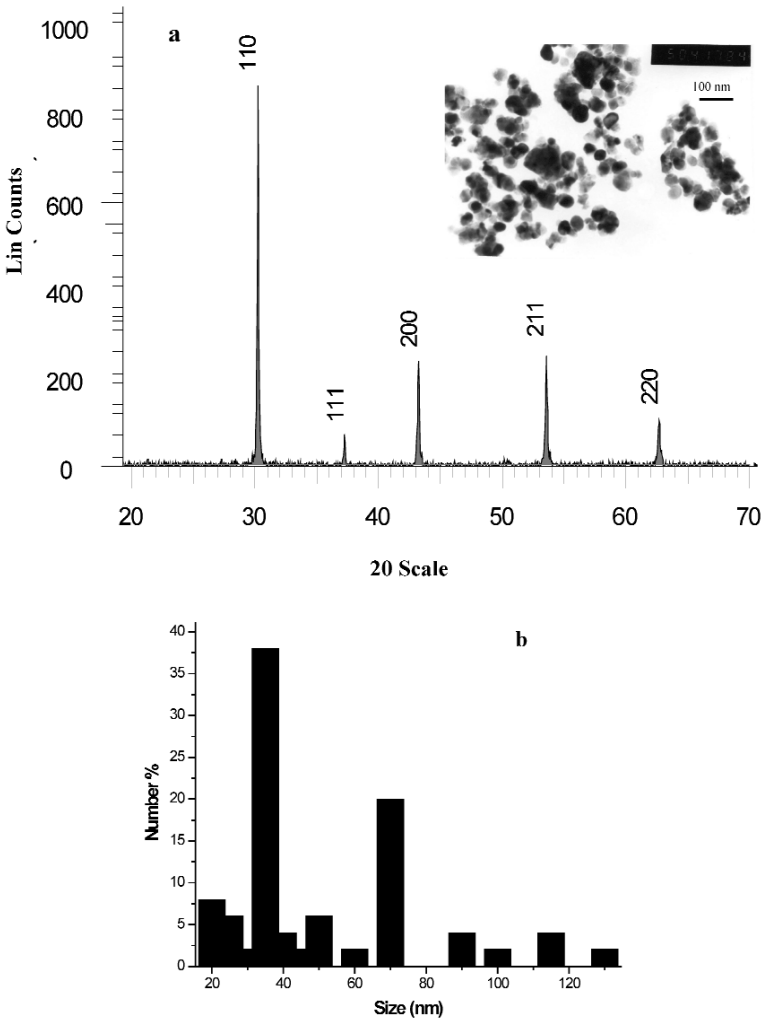

Fig. 10 (a) PXRD patterns of $BaZrO_3$ after calcining at 800 °C. Inset shows TEM micrographs of $BaZrO_3$ heated at 800 °C. (b) Size distribution plot of $BaZrO_3$.

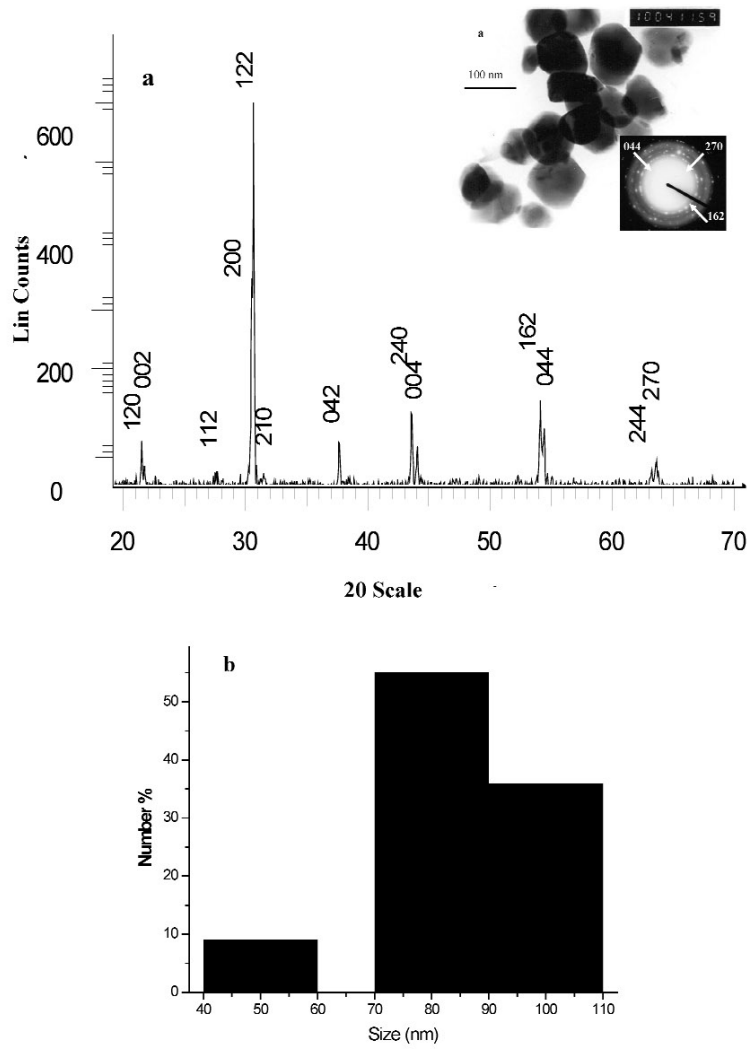

Fig. 11 (a) PXRD patterns of $PbZrO_3$ after calcining at 800 °C. Inset shows TEM micrographs of $PbZrO_3$ heated at 800 °C. Inset of TEM image shows the electron diffraction of $PbZrO_3$ powder heated at 800 °C. (b) Size distribution plot of $PbZrO_3$.

We also obtained the entire solid solution of $BaZrO_3$ and $PbZrO_3$ ($Ba_{1-x}Pb_xZrO_3$). The powder pattern corresponding to the $x = 0.25$ composition was indexed on a cubic cell similar to the pure $BaZrO_3$. The orthorhombic phase was observed at a higher value of x in $Ba_{1-x}Pb_xZrO_3$. The PXRD pattern (Fig. 12a) clearly shows additional reflections for the lead-rich region $0.50\ x \leq 1.00$ which was indexed in the orthorhombic unit cell known for $PbZrO_3$. The a, b, and c parameters decrease slightly with Pb content. The particle size increases with x. TEM micrographs for the solid solution are shown in the inset of Fig. 12a. Note that this was the first report [71] of the synthesis and properties of solid solution, $Ba_{1-x}Pb_xZrO_3$ (for $x = 0.25$, 0.50, and 0.75). The size distribution plot (calculated from TEM) is shown in Fig. 13.

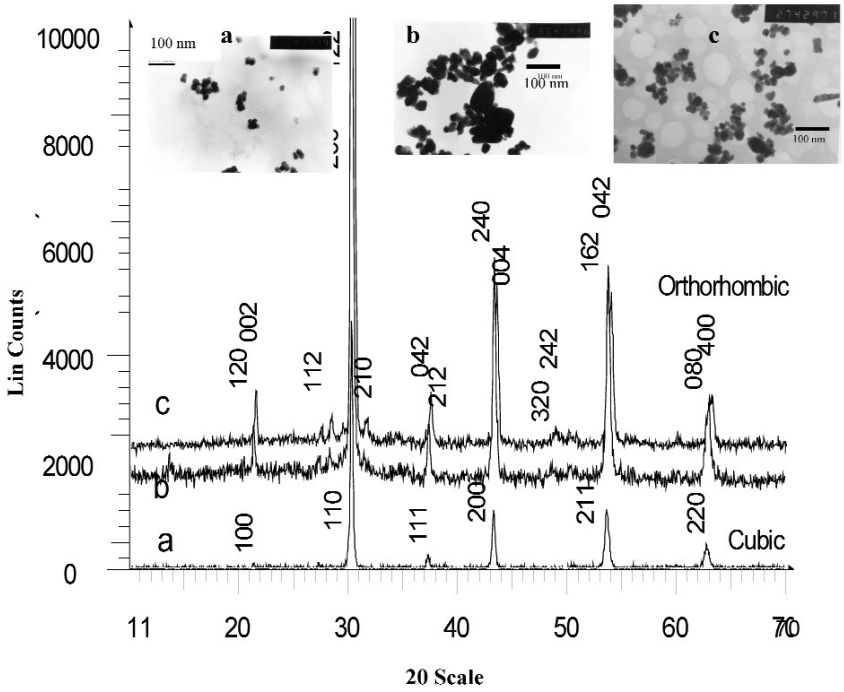

Fig. 12 (a) PXRD pattern of $Ba_{1-x}Pb_xZrO_3$ at (a) $x = 0.25$, (b) $x = 0.50$, and (c) $x = 0.75$ after calcining the powders at 800 °C. Inset shows TEM micrographs of $Ba_{1-x}Pb_xZrO_3$ with (a) $x = 0.25$, (b) $x = 0.50$, and (c) x = 0.75 heated at 800 °C.

We have also attempted to synthesize the high-pressure form of $CaCO_3$ (aragonite) at ambient pressure by the reverse micellar method (which creates conditions of high pressure, also called the Laplace pressure, inside the spheres). The lowest temperature for obtaining the aragonite phase in pure form is earlier reported to be 70 °C [72]. The reaction conditions were monitored with varying time periods and different temperatures to obtain pure $CaCO_3$. Low temperatures of 5–20 °C led to the formation of a mixture of vaterite and calcite phases (Fig. 13). The ratio of calcite to vaterite changed with aging time, for instance: 88 % of the vaterite phase was obtained after aging of 1 h (at 20 °C); the calcite phase becomes a major phase (74 %) after aging of 96 h (Fig. 14); after aging of 168 h, pure calcite phase is obtained. The inset of Fig. 13 shows the histogram of the same study. Thus, the digestion time of the reaction is an important factor for controlling the ratio of vaterite and calcite phase.

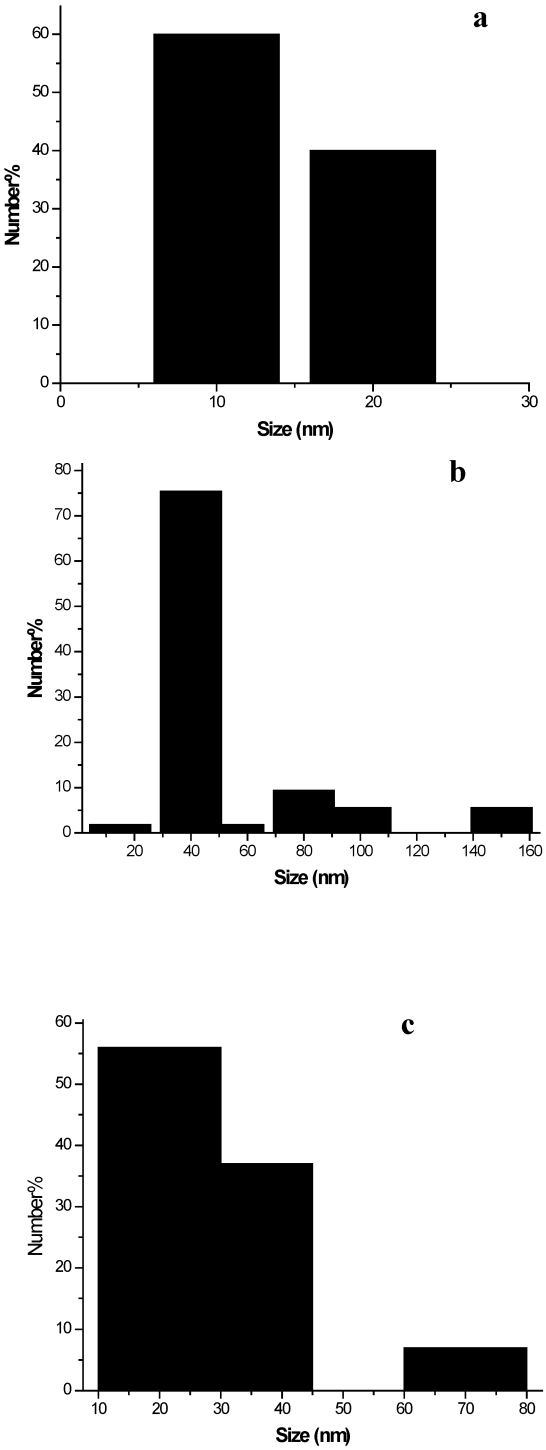

Fig. 13 Size distribution plot of $Ba_{1-x}Pb_xZrO_3$ at (a) $x = 0.25$, (b) $x = 0.50$, and (c) $x = 0.75$ after calcining the powders at 800 °C.

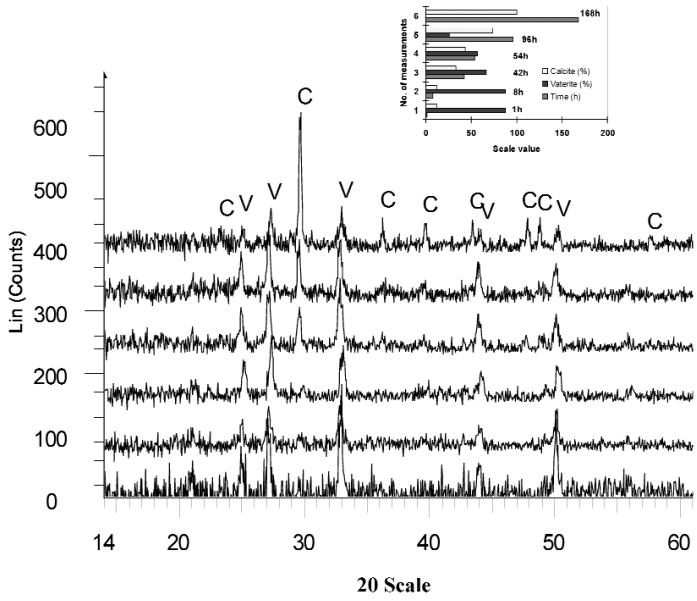

Fig. 14 Compositions of vaterite and calcite forms of calcium carbonate using (a) PXRD studies. Inset shows the histogram showing the exact composition with different aging time.

The reaction temperature was also varied from 40, 60, 70, and 85 °C. Under all the above temperature conditions, monophasic aragonite phase of $CaCO_3$ was obtained (Fig. 15). The aragonite phase (orthorhombic) is normally stabilized at high pressure and temperature [47]. Coprecipitation or any

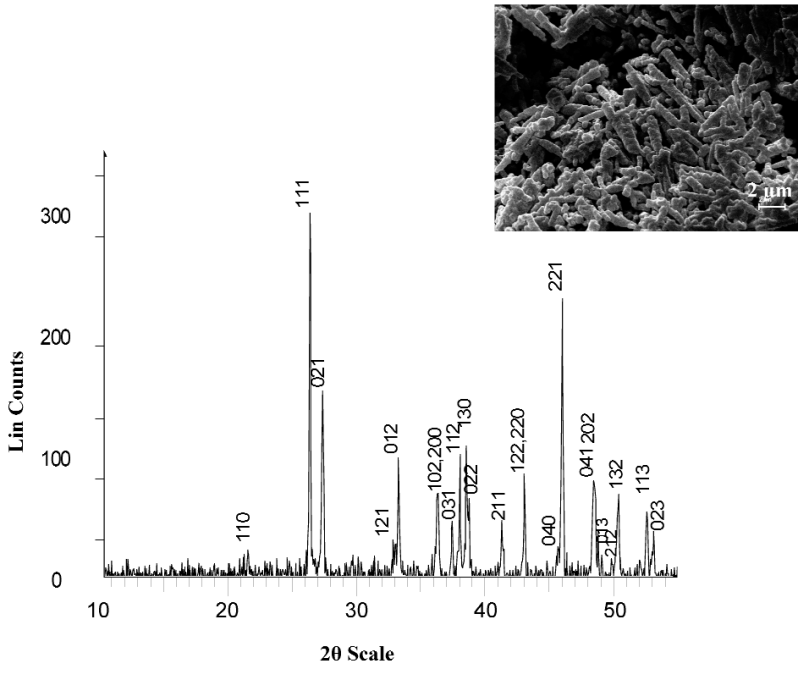

Fig. 15 PXRD of (a) calcium carbonate (aragonite) obtained at 40 °C after aging of 6 h. Inset shows the SEM micrographs of aragonite calcium carbonate obtained at 40 °C.

other low temperature (in the absence of high pressure) reaction of Ca^{2+} and carbonate ions at room temperature leads to the formation of calcite,which crystallizes in the rhombohedral structure [73,74]. We could obtain nanoparticles of aragonite with 100 % purity at reasonably low temperature (40–85 °C). The formation of a high-pressure phase stabilized at low temperature could be possibly due to the excess pressure generated inside the core of the reverse micelles [75]. Scanning electron microscopy (SEM) studies of aragonite synthesized at 40 °C (inset of Fig. 15) show that some of the nanorods form Y-junctions. However, increasing the temperature (up to 85 °C) leads to the loss of these junctions and only rods are observed (Fig. 16).

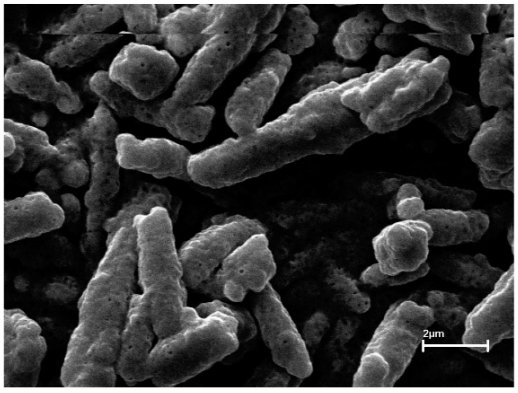

Fig. 16 SEM micrographs of calcium carbonate (aragonite) at 85 °C.

Pure calcite phase was obtained after aging of 168 h at 20 °C (Fig. 17). The same diffraction pattern of calcite is obtained at a reaction temperature of 105 °C. $CaCO_3$ (calcite) could also be obtained when aragonite $CaCO_3$ (orthorhombic) was heated at 550 °C. This transformation indicates that the stability of the orthorhombic phase requires high pressure along with high temperature. High temperature alone is not the key factor for the formation of aragonite, as mentioned in some earlier reports [47].

Thermogravimetric analysis and differential thermal analysis (TGA, DTA) show two distinct regions of weight loss. The first loss at 250 °C corresponds to the loss of two water molecules. The second weight loss at 710 °C corresponds to the decomposition of carbonate to pure calcium oxide. IR studies show the formation of $CaCO_3$ with characteristic sharp peaks at 1786, 854, and 713 cm^{-1} and a broad band at 1498 cm^{-1}. These peaks correspond to CO_3^{2-} vibrational frequencies [76]. The broad band at 3424 cm^{-1} could be assigned to the O–H stretching of water. Weak bands at 2920, 2851, 2523, and 2361 cm^{-1} may be due to the C–H stretching modes arising due to the surfactant molecules associated with the carbonate.

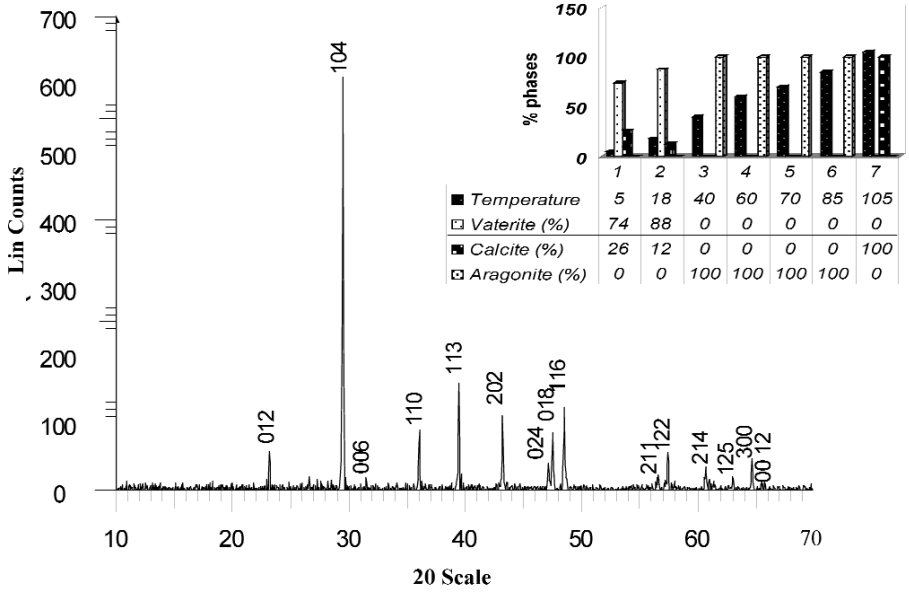

Fig. 17 Calcium carbonate (calcite) obtained after aging of 168 h at 20 °C using reverse micelles. The same diffraction pattern of calcite is obtained at a reaction temperature of 105 °C. Inset shows the histogram of various phases of calcium carbonate with reaction temperature in reverse micelles.

Properties

Gas sensing

The sensitivity of the SnO_2 nanopowder was tested using a 1000 ppm *n*-butane gas at 350 °C. A sensitivity of around 80.79 % with a fast recovery time of around 45 s was observed for SnO_2 nanoparticles (Table 3). Gas sensitivity is defined as $S = (R_A – R_G/R_A) \times 100$ % where R_A is the resistance in air and R_G is the resistance in the gas environment at the same temperature. The response of two different sensors fabricated using the same powder samples is shown in Table 3. The reason for the observed difference in the sensitivity is not very clear. The response was checked three times to confirm its reliability. It is to be noted that though relative humidity is reported to have detrimental effects on the gas sensing properties of polycrystalline SnO_2-based oxides in nanostructured SnO_2, these are found to have little impact. Pure SnO_2 is recognized as a poor sensing material for reducing gases such as butane, methane, etc. [77]. Small amounts of noble metals and ceramic oxides are added as catalysts to SnO_2 sensor materials to promote sensitivity [78]. Recently, an enhancement in the butane sensitivity of up to 91 % from the SnO_2 powders prepared by microwave treatment has been reported by Srivastava et al. [79]. Wang et al. reported the enhanced H_2 gas sensing properties of mesostructured SnO_2 powder prepared by using CTAB as the organic template [80]. They observed ethanol sensitivity under ambient conditions from nanoparticles of SnO_2 powders prepared by a solution route using polyvinyl pyrrolidone [64]. Thus, nanocrystalline tin oxides have been reported to have better performance as gas sensors due to the high surface/volume ratio and higher number of active sites for the oxidation/reduction process.

Table 3 1000 ppm butane gas sensitivity of SnO_2 nanoparticles.

R_A(MΩ)	R_G(MΩ)	Sensitivity (%)	Recovery time	Particle size
2.66	0.5109	80.79	45 s	8 nm
7.12	0.2290	67.83	1 min	8 nm

Dielectric properties

The dielectric properties were measured on sintered disks (Table 4). Dielectric properties for CeO_2 were measured on disks sintered at 800 and 1000 °C. The dielectric constant of the disk sintered at 800 °C was found to be ~19 at 500 kHz and dielectric loss ~0.11 at 500 kHz. The dielectric constant and dielectric loss were stable with frequency at room temperature. The dielectric constant was stable with temperature at 500 KHz. A minimum at 150 °C with a value of 0.028 was observed in the temperature variation studies of the dielectric loss. Dielectric properties of CeO_2 nanoparticles (synthesized from the oxalate precursor) sintered at 1000 °C were found to be stable with frequency. The dielectric constant (~15 at 500 kHz) was nearly stable with temperature. The dielectric loss (0.08 at 500 kHz) shows a constant value until 200 °C beyond which it rises sharply. The dielectric constant for bulk CeO_2 (with no mention of grain size and the sintering temperature) was earlier reported [81] to be 26.

Table 4 Summarized results of the dielectric measurements.

Compound	Particle size (TEM) (nm)	Frequency (kHz)	Sintering temperature (°C)	Dielectric constant ε	Dielectric loss D
$SrTiO_3$	50	100	1000	90	0.08
Sr_2TiO_4	20–25	100	1000	30	0.01
$BaTiO_3$	20–25	100	900	210	0.02
Ba_2TiO_4	150–200	100	1000	40	0.06
$SrZrO_3$	65–75	100	1000	19.8	0.01
$BaZrO_3$	25–30	100	1000	18.5	0.3
$PbZrO_3$	75	100	1000	30.5	0.02
$Ba_{0.75}Pb_{0.25}ZrO_3$	10–20	100	1000	76	0.01
$Ba_{0.5}Pb_{0.5}ZrO_3$	40	100	1000	93.3	0.09
$Ba_{0.25}Pb_{0.75}ZrO_3$	20–70	100	1000	69	0.09
CeO_2	Particles: 10		800	19	0.11
	Rod: 7 (d)	500			
	30 nm (l)		1000	~20	0.1
ZrO_2	3–5	500	1000	12	0.31

The dielectric properties for ZrO_2 nanoparticles, synthesized from the oxalate precursor, were measured on disks sintered at 1000 °C. The dielectric constant was ~12 at 500 kHz), and the loss was found to be ~0.31 at 500 kHz. Both dielectric constant and loss were highly stable with frequency at room temperature. The dielectric constant was stable after 100 °C, however, the dielectric loss falls to ~0.03 at 100 °C from 0.31 at room temperature. It has been reported [82] that the dielectric constant for pure monoclinic zirconia is ~22 at 10 kHz. Addition of 14 wt % CeO_2 to zirconia results in a mixture of monoclinic (44 %) and tetragonal phase, and the dielectric constant for this Ce-stabilized zirconia was reported to be 27 at 10 kHz. However, the doping of CaO to ZrO_2 led to the formation of 95 % tetragonal phase [82], and the dielectric constant increases to 34.

The dielectric constant for $SrTiO_3$ was found to be 90 and dielectric loss was 0.08 at 100 kHz. The dielectric constant was stable with frequency and temperature while dielectric loss showed an increase at higher frequencies. An earlier report on $SrTiO_3$ nanocrystals (48 nm) prepared by citrate precursor [83] method shows a dielectric constant of 190 and dielectric loss of 0.001 (at 100 kHz) at a sintering temperature of 1100 °C for 3 h. A dielectric constant of 363 for $SrTiO_3$ (210 nm, sintered at 1100 °C for 1 h) prepared by the oxalate precursor route [84] was reported. Thus, the synthetic route, sintering temperature, and grain size have strong influence on the dielectric constant.

For Sr_2TiO_4 prepared by the reverse-micellar route, the dielectric constant was found to be 30 at 100 kHz, which is stable with frequency and temperature while the dielectric loss (0.01 at 100 kHz) is also quite stable with frequency but increases beyond 200 °C. A study [85] on the dielectric properties

of Sr_2TiO_4 prepared by citrate method shows that the dielectric constant (ε) was 27. Note that the dielectric constant of ~35 was reported earlier [86] at 54 kHz for Sr_2TiO_4 obtained by sintering at 1650 °C, which probably leads to a much higher density. However, the sintering temperature is very high compared to our method, and the increase in dielectric constant is marginal.

The dielectric constant and loss of the nanostructured barium titanate was measured on sintered disks sintered at 900 °C as a function of frequency and temperature. The dielectric constant was found to be 210, and the dielectric loss was 0.02 at 100 kHz. The dielectric constant was stable with frequency and temperature while dielectric loss showed a slight increase at higher frequencies. Dielectric properties were also studied after sintering at 1000 and 1100 °C. The dielectric constant increased with sintering temperature (520 at 100 kHz after sintering at 1100 °C). The dielectric loss decreased with sintering temperature, which could be because of an increase in grain size. The dielectric constant reported by us is among the highest reported for nanostructured $BaTiO_3$ obtained by different routes [82]. In the temperature variation study for $BaTiO_3$ sintered at 1100 °C, a small peak was observed in the dielectric loss near 140–150 °C. The dielectric constant also shows a broad maximum (in the region 120–150 °C) in the 1100 °C sintered sample which may be associated with the ferroelectricity of $BaTiO_3$. The ferroelectricity found in $BaTiO_3$ (for micron-sized grains) appears as a peak in the dielectric constant at 122 °C. The transition was diffuse and weak in nanostructured $BaTiO_3$ (this study). Ferroelectricity depends on grain size as has been shown earlier by theoretical calculations [87,88]. These calculations predict a critical grain size of the order of 44 nm in $BaTiO_3$. It has been shown recently that ferroelectricity may be observed in defect-free ultra-thin films [89,90] much below (<10 nm) the limits normally suggested by a mean-field Ginzburg–Landau approach.

The dielectric constant of pure orthorhombic Ba_2TiO_4 (obtained after sintering at 1000 °C) was 40, and the loss was 0.06 at 100 kHz. The dielectric constant is stable with frequency but decreases with temperature from 39 (at 30 °C) to 20 (at 100 °C), beyond which it remains stable. The dielectric constant of orthorhombic Ba_2TiO_4 sintered at 1200 °C and annealed in argon is reported [91] to be 1300 at 1 kHz. We obtained a much lower value of 51 at 100 kHz, which could be because of higher sintering temperature in the above study leading to larger grain sizes. The dielectric properties of the pure monoclinic form of Ba_2TiO_4 are yet unknown.

The value of dielectric constant and loss for $SrZrO_3$ was found to be 19.8 and 0.01, respectively, at room temperature and at 100 kHz. The dielectric constant was stable with frequency and temperature. The dielectric constant of bulk $SrZrO_3$, obtained using the solid-state route (4–5 μm, sintered at 1450 °C for 2 h) is reported to be around 26.5 [92]. However, there is no report available on the dielectric properties of nanocrystalline strontium zirconate synthesized using the reverse micellar route.

The dielectric constant was found to be 18.5 for $BaZrO_3$, which is lower than the values reported earlier (ranging from 32 to 36 depending on the sintering temperature and method of synthesis) [93–95]. The variation of dielectric constant with temperature was also marginal. The dielectric loss was found to steadily decrease with frequency. The dielectric constant for (a) $x = 0.25$ was found to be 76 and dielectric loss was 0.01 The dielectric constant decreased with temperature until 150 °C, was stable after that, however, the dielectric loss increases slightly at higher temperature, (b) $x = 0.5$, the dielectric constant was 93.3 and dielectric loss was 0.09. The dielectric constant and dielectric loss were stable with frequency while the loss decreased with temperature until 100 °C and thereafter remains constant up to 200 °C, (c) $x = 0.75$, the dielectric constant was found to be 69 at 100 kHz, which is stable with frequency, and the loss was found to be 0.09. All the values of dielectric constant and loss are reported at 100 kHz. For pure $PbZrO_3$, the dielectric constant was 30.5, and the dielectric loss was 0.02 at 100 kHz. The dielectric constant was stable with frequency, and the dielectric loss was stable at lower frequency and increases slightly at higher frequencies (400–500 kHz). The dielectric constant has a maximum at around 230 °C, which corresponds to the AFE to paraelectric (PE) phase transition in $PbZrO_3$ [92]. The dielectric constant (at room temperature and at 100 kHz frequency) increases up to $x = 0.50$. Thereafter, it decreases steadily. In earlier studies [96–99] strong influence of the introduction of Pb ions onto the Ba sublattice on the antiferroelectric–ferroelectric (AFE–FE) and FE–PE phase-transition temperatures

and compositional width of the FE phase has been reported for $(Ba_{1-x}Pb_x)ZrO_3$ with $x > 0.65$. In our studies, no AFE → PE transition was observed in any of the compositions except for the pure $PbZrO_3$. Two very distinct ranges of the Pb content, for $x < 0.9$ and $x > 0.9$ of bulk $Ba_{1-x}Pb_xZrO_3$ was observed, at which the properties are substantially different [97]. It was shown that the best dielectric properties occurs in ceramics with $x = 0.9$. The dielectric properties of nanocrystalline $Ba_{1-x}Pb_xZrO_3$ ($0 \le x \le 1$) over the entire range of x values were shown by us for the first time [71]. We have also shown the presence of a maximum in the dielectric constant with Pb content corresponding to the $x = 0.5$ composition, which may be due to the presence of a structural phase transition close to this composition.

CONCLUSIONS

Reverse micelles have been found to be a versatile route for the synthesis of nanoparticles of various oxides. The particles obtained are homogeneous and monophasic. $SrTiO_3$ and Sr_2TiO_4 with grain size of 40 and 30 nm, respectively, were synthesized using this methodology. Nanometer-sized (20–25 nm) barium titanate was also synthesized by a modified reverse micellar route (avoiding Ba-alkoxide) at 800 °C. Monodisperse and nearly uniform grains were obtained at this low temperature. A weak (diffuse) FE behavior in the dielectric constant of nanocrystalline $BaTiO_3$ sintered at 1100 °C is observed with a dielectric constant of 520. Monophasic nanocrystalline oxides belonging to the solid solution of the type $Ba_{1-x}Pb_xZrO_3$ ($0 \le x \le 1$) with grain size in the range of 20–60 nm were obtained at 800 °C. A structural phase transition in the region between $x = 0.25$ to 0.5 from cubic to orthorhombic structure was observed. The grain size increases with the lead content in $Ba_{1-x}Pb_xZrO_3$ ($0 \le x \le 1$). The dielectric constant of the solid solution of $Ba_{1-x}Pb_xZrO_3$ ($0 \le x \le 1$) shows a maximum value of 93 for $x =$ 0.50. Nanocystalline ceria (crystallite size of 15 nm) and zirconia (3–5 nm) could be obtained at 500 °C from oxalate precursor which was synthesized using reverse micelles. Enhanced gas sensitivity towards *n*-butane was observed from the nanoparticles of SnO_2 (8 nm) prepared by us compared to the polycrystalline SnO_2 samples prepared by other solution-phase techniques. The aragonite type of calcium carbonate was synthesized at low temperature of 40 °C using reverse micelles. Overall, we conclude that our studies show the great potential of the reverse micellar route to provide a variety of nanomaterials.

REFERENCES

1. L. N. Lewis. *Chem. Rev*. **93**, 2693 (1993).
2. A. P. Alivisatos. *Science* **271**, 933 (1996).
3. D. L. Feldheim, C. D. Keating. *Chem. Soc. Rev.* **27**, 1 (1998).
4. W. P. McConnell, J. P. Nowak, L. C. Brousseau, R. R. Fuierer, R. C. Tenent, D. L. Feldheim. *J. Phys. Chem. B* **104**, 8925 (2000).
5. T. Trindade, P. O'Brien, N. L. Pickett. *Chem. Mater*. **13**, 3843 (2001).
6. S. C. Farmer, T. E. Patten. *Chem. Mater.* **13**, 3920 (2001).
7. X. J. Xu, P. Y. Chow, L. M. Gan. *J. Nanosci. Nanotechnol*. **2**, 61 (2002).
8. C. Feldmann, H.-O. Jungk. *Angew. Chem., Int. Ed*. **40**, 359 (2001).
9. Y. Volokitin, J. Sinzig, L. J. de Jongh, G. Schmid, M. N. Vargaftik, I. I. Moiseev. *Nature* **384**, 621 (1996).
10. K. Holmberg. *Handbook of Applied Surface and Colloid Chemistry*, Vols. I–II, John Wiley, New York (2001).
11. R. S. Niranjan, Y. K. Hwang, D. K. Kim, S. H. Jhung, J. S. Chang, I. S. Mulla. *Mater. Chem. Phys.* **92**, 384 (2005).
12. S. Schiller, U. Heisig, K. Goedicke, H. Bilz, K. Steinfelder. *Thin Solid Films* **92**, 81 (1982).
13. S. C. Lee, J. H. Lee, T. S. Oh, Y. H. Kim. *Sol. Energy Mater. Sol. Cells* **75**, 481 (2003).

14. T. Stergiopoulos, I. M. Arabatzis, H. Cachet, P. Falaras. *J. Photochem. Photobiol., A* **155**, 481 (2003).
15. D. Aurbach, A. Nimberger, B. Markovasky, E. Levi, E. Sominsky, A. Gedanken. *Chem. Mater.* **14**, 4155 (2002).
16. M. Miyauchi, A. Nikajima, T. Watanabe, K. Hasimoto. *Chem. Mater.* **14**, 2812 (2002).
17. G.-J. Li, S. Kawi. *Mater. Lett.* **34**, 99 (1998).
18. B. C. H. Steele, A. Heinzel. *Nature* **414**, 345 (2001).
19. F. H. Garzon, R. Mukundan, E. L. Brosha. *Solid State Ionics* **136–137**, 633 (2000).
20. R. Dimonte, P. Fornasiero, M. Graziani, J. Kašpar. *J. Alloys Compd.* **275–277**, 877 (1998).
21. B. Elidrissi, M. Addou, M. Regragui, C. Monty, A. Bougrine, A. Kachouane. *Thin Solid Films* **379**, 23 (2000).
22. M. Fujimoto, W. D. Kingery. *J. Am. Ceram. Soc*. **68**, 169 (1985).
23. S. H. Kim, J. D. Byun, W. Park, Y. Kim. *J. Mater. Sci.* **34**, 3057 (1999).
24. J. C. C. Abrantes, J. A. Labrincha, J. R. Frade. *J. Eur. Ceram. Soc*. **20**, 1603 (2000).
25. A. Kudo, A. Tanaka, K. Domen, T. Onishi, K. Tamaru. *J. Catal*. **111**, 296 (1988).
26. A. Beauger, J. C. Mutin, J. C. Niepce. *J. Mater. Sci.* **18**, 3041 (1983).
27. A. Beauger, J. C. Mutin, J. C. Niepce. *J. Mater. Sci*. **18**, 3543 (1983).
28. A. Beauger, J. C. Mutin, J. C. Niepce. *J. Mater. Sci*. **19**, 195 (1984).
29. T. Osaka, C. Numako, K. Koto. *Mater. Res. Bull*. **34**, 11 (1999).
30. V. Longo, F. Richiasdiello, O. Shaizero, R. Carlsson, S. Carlsson (Eds.). *Swedish Ceram. Soc.* 467 (1981).
31. J. Nair, P. Nair, E. B. M. Doesburg, J. G. Van Ommen, J. R. H. Ross, A. J. Burggraaf, F. Mizukmi. *J. Mater. Sci.* **33**, 4517 (1998).
32. B. J. Kennedy, C. J. Howard, B. C. Chakoumakos. *Phys. Rev. B* **59**, 4023 (1999).
33. T. Yajima, H. Suzuki, T. Yoyo, H. Iwahara. *Solid State Ionics* **51**, 101 (1992).
34. T. Yamaguchi, Y. Komatsu, T. Otobe, Y. Murakami. *Ferroelectrics* **27**, 273 (1980).
35. H. Stetson, B. Schwartz. *J. Am. Ceram. Soc.* **44**, 420 (1961).
36. I. Levin, T. G. Amos, S. M. Bell, L. Farber, T. A. Vanderah, R. S. Roth, B. H. Toby. *J. Solid State Chem.* **175**, 170 (2003).
37. G. Shirane, S. Swaguchio, T. Tokagi. *Phys. Rev. B* **84**, 476 (1951).
38. H. D. Megaw. *Proc. Phys. Soc. London* **58**, 133 (1946).
39. E. E. Oren, E. Taspinar, A. C. Tas. *J. Am. Ceram. Soc.* **80**, 2714 (1997).
40. G. Shirane. *Phys. Rev.* **86**, 219 (1952).
41. B. P. Pokharel, D. Pandey. *J. Appl. Phys.* **88**, 5364 (2000).
42. S. Roberts. *J. Am. Ceram. Soc.* **33**, 63 (1950).
43. S. Mann, G. A. Ozin. *Nature* **382**, 313 (1996)
44. H. Yang, N. Coombs, G. A. Ozin. *Nature* **386**, 692 (1997).
45. T. S. Ahmadi, Z. L. Wang, T. C. Green, A. Henglein, M. A. El-Sayed. *Science* **272**, 1924 (1996).
46. C. M. Zaremba, A. M. Belcher, M. Fritz, Y. Li, S. Mann, P. K. Hansma, D. E. Morse, J. S. Speck, G. D. Stucky. *Chem. Mater.* **8**, 679 (1996).
47. K. Suito, J. Namba, T. Horikawa, Y. Taniguchi, N. Sakurai, M. Kobayashi, A. Onodera, O. Shimomura, T. Kikegawa. *Am. Mineral.* **86**, 997 (2001).
48. M. Gotic, I. C. Nagy, S. Popovic, S. Music. *Philos. Mag. Lett.* **78**, 193 (1998).
49. J. E. Schaefer, H. Kisker, H. Kronmuller, R. Wurschum. *Nanostruct. Mater.* **1**, 523 (1992).
50. S. D. Sartale, C. D. Lokhande. *Indian J. Eng. Mater. Sci*. **7**, 404 (2000).
51. U. Erb. *Nanostruct. Mater*. **6**, 533 (1995).
52. S. Komarneni, M. C. D'Arrigo, C. Leionelli, G. C. Pellacani, H. Katsuki. *J. Am. Ceram. Soc.* **81**, 3041 (1998).
53. A. Chatterjee, D. Das, S. K. Pradhan, D. Chakravorty. *J. Magn. Magn. Mater.* **127**, 214 (1993).
54. M. Boutonnet, J. Kizling, P. Stenius, G. Maire. *Colloids Surf.* **5**, 209 (1982).

55. M. P. Pileni, L. Motte, C. Petit. *Chem. Mater*. **4**, 338 (1992).
56. T. Ahmad, G. Kavitha, C. Narayana, A. K. Ganguli. *J. Mater. Res.* **20**, 1415 (2005).
57. T. Ahmad, A. K. Ganguli. *J. Mater. Res.* **19**, 2905 (2004).
58. I. Lisiecki, M. P. Pileni. *J. Am. Chem. Soc.* **115**, 3887 (1993).
59. J. P. Wilcoxon, R. L. Williamson, R. Baughman. *J. Chem. Phys.* **98**, 9933 (1993).
60. K. Osseo-Asare, F. J. Arriagada. *Colloids Surf.* **50**, 321 (1990).
61. H. Herrig, R. Hempelmann. *Nanostruct. Mater*. **9**, 241 (1997).
62. A. R. Koran, R. Hull, R. L. Opila, M. G. Bawendi, M. L. Steigerwald, P. J. Carroll, L. E. Brus. *J. Am. Chem. Soc.* **112**, 1327 (1990).
63. T. Ahmad, G. Kavitha, C. Narayana, A. K. Ganguli. *J. Mater. Res*. **20**, 1415, (2005).
64. Y. Wang, X. Jiang, Y. Xia. *J. Am. Ceram. Soc*. **125**, 16176 (2003).
65. C. P. Sibu, S. Rajesh Kumar, P. Mukundan, K. G. K. Warrier. *Chem. Mater.* **14**, 2876 (2002).
66. R. A. MacPhail, H. L. Strauss, R. G. Snyder. *J. Phys. Chem.* **88**, 334 (1984).
67. A. G. Pereira, A. O. Porto, G. M. de Lima, H. G. L. Siebald, J. D. Ardission. *Solid State Commun*. **127**, 223 (2003).
68. C. Beck, W. Haartl, R. Hempelmann. *J. Mater. Res*. **13**, 3174 (1998).
69. H. Herrig, R. Hempelmann. *Mater. Lett.* **27**, 287 (1996).
70. J. Wang, J. Fang, S. C. Ng, L. M. Gan, C. H. Chew, X. Wang, Z. Shen. *J. Am. Ceram. Soc.* **82**, 873 (1999).
71. T. Ahmad, A. K. Ganguli. *J. Am. Ceram. Soc.* **89**, 3140 (2006).
72. J. L. Wray, F. Daniels. *J. Am. Chem. Soc.* **79**, 2031 (1957).
73. S. Hirano, H. Kuroda, R. Toyokuni. Eur. Patent Appl. 88-303407 (1988).
74. I. V. Nefyodova, V. I. Borodin, P. P. Chvanski, N. I. Leonyuk, *J. Cryst. Growth* **211**, 458 (2000).
75. S. Nad, P. Sharma, I. Roy, A. Maitra. *J. Colloid Interface Sci.* **264**, 89 (2003).
76. C. Viravaidya, M. Li, S. Mann. *Chem. Commun*. **19**, 2182 (2004).
77. G. Eranna, B. C. Joshi, D. P. Runthala, R. P. Gupta. *Crit. Rev. Solid State Mater. Sci.* **29**, 111 (2004).
78. K. Cahtterjee, S. Chatterjee, A. Banerjee, M. Raut, N. C. Pal, A. Sen, H. S. Maiti. *Mater. Chem. Phys.* **81**, 33 (2003).
79. A. Srivastava, K. Jain Rashmi, A. K. Srivastava, S. T. Lakshmikumar. *Mater. Chem. Phys.* **97**, 85 (2006).
80. Y. Wang, X. Wu, Y. Li, Z. Zhou. *Solid State Electron.* **48**, 627 (2004).
81. S. Logothetidis, P. Patsalas, E. K. Evangelou, N. Konofaos, I. Tsiaoussis, N. Frangis. *Mater. Sci. Eng. B* **109**, 69 (2004).
82. D. P. Thompson, A. M. Dickins, J. S. Thorp. *J. Mater. Sci.* **27**, 2267 (1992).
83. P. R. Arya, P. Jha, A. K. Ganguli. *J. Mater. Chem*. **13**, 415 (2003).
84. M. A. Sekar, G. Dhanaraj, H. L. Bhat, K. C. Patil. *J. Mater. Sci.: Mater. Electron.* **3**, 237 (1992).
85. V. Shanker, T. Ahmad, A. K. Ganguli. *Bull. Mater. Sci.* **27**, 421 (2004).
86. J. H. Sohn, Y. Inaguma, M. Itoh, T. Nakamura. *Mater. Sci. Eng., B* **41**, 50 (1996).
87. Y. G. Wang, W. L. Zhong, P. L. Zhang. *Solid State Commun*. **90**, 329 (1994).
88. K. Binder. *Ferroelectrics* **35**, 99 (1981).
89. T. Tybell, C. H. Ahn, J. M. Triscone. *Appl. Phys. Lett*. **75**, 856 (1999).
90. J. Junquera, P. Ghosez. *Nature* **422**, 506 (2003).
91. G. Pfaff. *J. Mater. Sci. Lett*. **10**, 1059 (1991).
92. H. Stetson, B. Schwartz. *J. Am. Ceram. Soc*. **44**, 420 (1961).
93. T. Yamaguchi, Y. Komatsu, T. Otobe, Y. Murakami. *Ferroelectrics* **27**, 273 (1980).
94. I. Levin, T. G. Amos, S. M. Bell, L. Farber, T. A. Vanderah, R. S. Roth, B. H. Toby. *J. Solid State Chem*. **175**, 170 (2003).
95. H. Fujishita, Y. Shiozaki, N. Achiwa, E. Sawaguchi. *J. Phys. Soc. Jpn*. **51**, 3583 (1982).
96. B. P. Pokharel, D. Pandey. *J. Appl. Phys.* **88**, 5364 (2000).

97. Z. Ujma, J. Handerek, M. Pawelczyk, D. Dmytrow. *Ferroelectrics* **129**, 127 (1992).
98. I. El-Harrad, P. Becker, C. C. Nedelec, J. Handerek, Z. Ujma, D. Dmytrow. *Vib. Spectrosc.* **10**, 301 (1996).
99. B. P. Pokharel, D. Pandey. *J. Appl. Phys*. **90**, 2985 (2001).